Energy & Environmental Science

PAPER

View Article Online
View Journal

Cite this: DOI: 10.1039/c8ee00595h

Flexible three-dimensional interconnected piezoelectric ceramic foam based composites for highly efficient concurrent mechanical and thermal energy harvesting†

Guangzu Zhang, ‡[ab] Peng Zhao, ‡[c] Xiaoshan Zhang, [b] Kuo Han, [b] Tiankai Zhao, [c] Yong Zhang, [b] Chang Kyu Jeong, [bd] Shenglin Jiang, [a] Sulin Zhang *[c] and Qing Wang *[b]

Received 22nd February 2018,
Accepted 20th April 2018

DOI: 10.1039/c8ee00595h

rsc.li/ees

Flexible piezoelectric materials are pivotal to a variety of emerging applications ranging from wearable electronic devices, sensors to biomedical devices. Current ceramic-polymer composites with embedded low-dimensional ceramic fillers, though mechanically flexible, suffer from low piezoelectricity owing to the poor load-transfer efficiency that typically scales with the stiffness ratio of the polymer matrix to the ceramic fillers. Herein we introduce the scalable ceramic-polymer composites based on three-dimensional (3-D) interconnected piezoelectric microfoams. Comprehensive mechanics analyses reveal that the 3-D interconnected architecture presents a continuous pathway for load transfer to break the load-transfer scaling law seen in the conventional composites with low-dimensional ceramic fillers. The 3-D composite exhibits exceptional piezoelectric characteristics under multiple loading conditions (*i.e.*, compression, stretching, and bending) and high mechanical durability under thousands of cycles. The 3-D composite also displays excellent pyroelectricity, thereby enabling concurrent thermal and mechanical energy scavenging. Our findings suggest an innovative material framework for high-performance energy harvesters and self-powered micromechanical devices.

Broader context

Multifunctionality, mechanically flexibility and durability, and scalability are highly desired attributes for piezoelectric materials to enable a variety of potential applications in advanced electronics and biomedical devices. An intuitive yet logical approach toward flexible piezoelectric materials is the development of ceramic-polymer composites. However, large stiffness disparity of the material constituents and the spatial discontinuity of the ceramic phase in the current piezoelectric-polymer nanocomposites, which are based on the low-dimensional (*i.e.* nanoparticles and nanowires) ceramic inclusions, render fairly poor load transfer from the surrounding polymer matrix to the active ceramic fillers, and thus significantly limiting their energy harvesting performance. Herein we introduce a unique class of the ceramic-polymer composite consisting of three-dimensional (3-D) interconnected piezoelectric microfoams in polydimethylsiloxane matrix. As proven in comprehensive mechanics analyses, the 3-D interconnected architecture breaks the load-transfer scaling law seen in the composites with low-dimensional ceramic fillers and provides a continuous pathway for a very high efficiency of load transfer. Consequently, the 3-D composite exhibits exceptional piezoelectric characteristics under multiple loading conditions. We further demonstrate excellent pyroelectricity from the 3-D composites, thereby enabling concurrent thermal and mechanical energy scavenging. The comprehensive experimental and simulation studies validate the 3-D composite as a new paradigm for the design of high-performance flexible energy-harvesting materials.

1. Introduction

Integration of mechanical flexibility into energy harvesting materials presents an emerging development trajectory toward a wide range of applications, such as sensory skins for robotics, artificial muscles, self-powered sensors, and wearable devices, *etc.*[1–3] Piezoelectric materials are particularly attractive because they offer an efficient route to scavenge energies from the living environment, such as human activities, to power mobile consumer electronics and nanosystems.[4–6] In addition to piezoelectricity, mechanical flexibility and cost-effective scalability are key matrices

[a] School of Optical and Electronic Information, Huazhong University of Science and Technology, Wuhan, Hubei 430074, P. R. China
[b] Department of Materials Science and Engineering, The Pennsylvania State University, University Park, Pennsylvania, 16802, USA. E-mail: wang@matse.psu.edu
[c] Department of Engineering Science and Mechanics, The Pennsylvania State University, University Park, Pennsylvania, 16802, USA. E-mail: suz10@engr.psu.edu
[d] Division of Advanced Materials Engineering, Chonbuk National University, Jeonju, Jeonbuk 54896, Republic of Korea

† Electronic supplementary information (ESI) available: Structural characterizations, more electrical property measurements and simulation analysis. See DOI: 10.1039/c8ee00595h

‡ These authors contributed equally to this work.

for these energy-harvesting materials.[7–9] However, mechanical flexibility and piezoelectricity appear to be two conflicting properties, as improving one often compromises the other.[1] Ferroelectric polymers, such as poly(vinylidene fluoride) and its copolymers, are mechanically flexible and easily processable,[10–14] but their piezoelectric coefficients are over one order of magnitude less than their ceramic counterparts.[15] Piezoceramics and single crystals with high piezoelectric coefficients, on the other hand, are very fragile, prone to fracture upon mechanical deformation and difficult to be processed into mechanically compliant structures.[16] To improve mechanical flexibility, high-density nanowire arrays[17–20] and thin films[21–26] of piezoelectric ceramics and piezoelectric semiconductor oxides[27–29] have been extensively explored. However, these one- and two-dimensional (1-D and 2-D) nanostructures are cost-ineffective for scalable production. Their low dimensions also limit the loading directions with considerable piezoelectric effects.

An intuitive yet logical approach toward flexible piezoelectric materials is the development of ceramic-polymer composites with piezoelectric ceramic nanostructures dispersed in polymer matrix.[30–36] Such composites are expected to combine excellent piezoelectricity of electroceramics with mechanical flexibility of polymers. Various competitive attributes and parameters, including the volume fraction and the morphology of the piezoelectric ceramics, dictate the combined mechano-piezoelectric responses of the composites. For example, increasing the piezoelectric ceramic fraction improves the piezoelectric effect,[37] but necessarily compromises mechanical flexibility of the resulting composites. The currently available piezoelectric-polymer nanocomposites are commonly based on the low-dimensional (0-D nanoparticles and 1-D nanowires) ceramic fillers.[3,37,38] However, the large stiffness disparity of the material constituents and the spatial discontinuity of the ceramic phase in these composites render fairly poor load transfer from the surrounding polymer matrix to the active ceramic fillers, and thus significantly limiting their piezoelectricity.[37,39–43]

Herein we introduce a facile and scalable approach to a new class of high-performance flexible polymer composites consisting of 3-D cellular-structured lead zirconate titanate (PZT) ceramic foam filled with polydimethylsiloxane (PDMS). Different from the low-dimensional ceramic filler based composites, the 3-D interconnected architecture of the PZT foam renders highly effective load transfer, which is independent of the relative stiffness of material constituents in the composite and of the loading directions. These features lead to significantly improved piezoelectricity under multiple deformation modes (*i.e.*, compression, stretching, and bending) as compared to the corresponding low-dimensional PZT based polymer composites. Moreover, the 3-D composite is mechanically flexible and durable, and able to sustain thousands of loading/unloading cycles without noticeable degradation. The composite also exhibits superior pyroelectricity, thereby enabling simultaneous thermal and mechanical energy harvesting.

2. Results and discussion

2.1 Preparation of 3-D PZT microfoam based composites

Fig. 1a and ESI,† Fig. S5, S6 illustrate the fabrication of the 3-D PZT composites, consisting of three main steps: (i) immersing polyurethane (PU) foam templates into the PZT sol; (ii) drying the sol and sintering the precursor to yield the 3-D PZT ceramic microfoams; (iii) filling PDMS into the 3-D PZT ceramic microfoams to form the composites. During the high-temperature sintering process, the PU templates and solvent in the PZT gel are volatilized, while the morphology of the templates is preserved in the ceramic foams with a ~150% shrinkage (Fig. 1b–d and ESI,† Fig. S5c, S7). As shown in the scanning electron microscopic (SEM) images (Fig. 1b–d), the 3-D PZT ceramic microfoams feature interconnected pores with an average pore size of ~100 μm and continuous PZT skeletons with a characteristic thickness of ~20 μm. The dense ceramic skeletons consist of uniform grains with an average grain size of 2 μm, as evidenced by the magnified SEM images (Fig. 1c and d). The energy dispersive spectroscopy (EDS) mapping (Fig. 1e), electron probe microanalysis (EPMA, ESI,† Fig. S8 and Table S2) and X-ray photoelectron spectroscopy (XPS, ESI,† Fig. S9) confirm that the elements of lead, zirconium, and titanium are homogeneously dispersed in the skeletons with the composition of $Pb(Zr_{0.52}Ti_{0.48})O_3$. The distinct diffraction peaks in the X-ray diffraction (XRD) patterns (ESI,† Fig. S10 and S11) suggest a tetragonal phase of the 3-D PZT ceramic microfoam. The volume fraction of the PZT ceramic skeletons is ~16% in the polymer composites. As shown in Fig. 1f, the 3-D composites can be stretched and bent by fingers with ease without fracture, and are highly conformable to different parts of human body, *e.g.*, shoulders and knees, suggesting their applicability in wearable devices. Our preparation process is versatile, *e.g.*, the size of the composites can be easily scaled up by using large PU foam templates, as demonstrated in Fig. 1f.

2.2 Piezoelectric energy harvesting

The piezoelectric responses of the 3-D composites (1 mm thick) were measured under periodically applied pressing–releasing cycles (Fig. 2). Considerable strain-dependent piezoelectric signals were attained after poling, as shown in ESI,† Fig. S13. The generated voltage and current are proportional to the applied strain (Fig. 2a). For example, under 8% applied strain, an output voltage (V_{out}) of ~85 V and current (I_{out}) of ~40 nA were obtained in the 3-D composites. These values are remarkably higher than the corresponding polymer composites with low-dimensional PZT fillers, which is consistent with the polarization–electric field (*P*–*E*) loops. The polarization of the 3-D composite is found to be considerably higher than those of the composites with low-dimensional PZT fillers (ESI,† Fig. S14).

To confirm that the measured output signals were indeed generated from the piezoelectric effect, we carried out the switching-polarity tests and linear superposition measurements. The 3-D composites clearly produced positive voltage at the pressing state when they were forwardly connected to the measurement instruments, but negative pluses when the connection was reversed (ESI,† Fig. S15). In addition, we observed negligible signals for the 3-D composites before electric poling (ESI,† Fig. S13). In the linear superposition measurements, two identical 3-D composites were integrated in serial and parallel connections, respectively. A V_{out} of ~40 V and an I_{out} of ~18 nA, about doubled those of individual composites, were generated

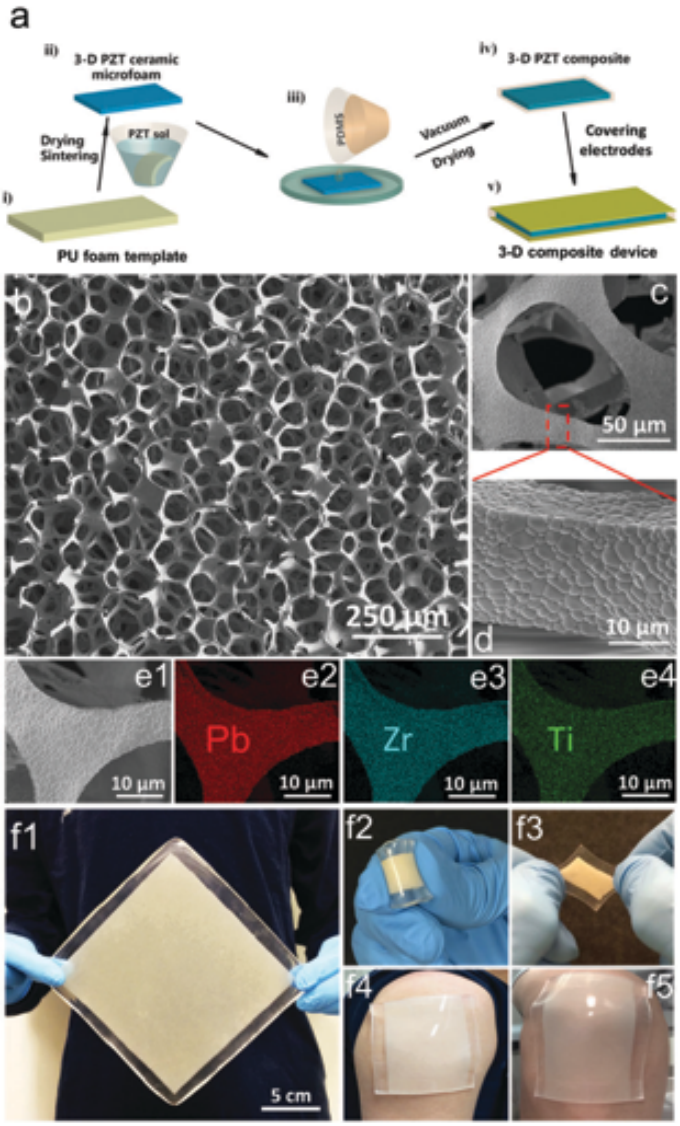

Fig. 1 Fabrication and structures of the 3-D polymer composites. (a) The schematics of the preparation procedure of the 3-D composites. (b) The SEM image of the 3-D PZT ceramic microfoams. (c) The magnified SEM image of the PZT skeletons. (d) The localized surface morphology of the skeleton. (e) The EDS mappings of the PZT skeleton. The elements of lead, zirconium and titanium are homogeneously dispersed in the skeletons. (f) The optical images of the 3-D composites. (f1) A large-area 3-D composite, demonstrating the scalability of the fabrication method for the 3-D ceramic composites. (f2 and f3) The 3-D composite bent and stretched by fingers. (f4 and f5) The 3-D composite attached on shoulder and knee, showing its mechanical flexibility and good compatibility with various parts of human body.

by the linearly superimposed composites under a 2% compressive strain (Fig. 2a and ESI,† Fig. S16). These findings not only confirm that the obtained outputs are the signals from the piezoelectric effect, but also demonstrate that the output voltages and currents can be tailored by integrating the composites in serial or parallel.

The piezoelectric responses can be seen clearly through finite element modeling of the strain and electric potential in the composites (Fig. 2b–d). In our model, the 3-D PZT microfoams were modeled as an isotropic elastic material with the polarization direction normal to the surface of the composites. The crystal symmetry and elastic isotropy of the PZT foams render only 3, 2, and 2 independent piezoelectric, dielectric, and elastic constants, respectively (ESI,† Table S1). The PDMS matrix, on the other hand, was modeled as an isotropic elastic material without piezoelectric effect. The PZT–PDMS interfaces were assumed to be seamless. The Weaire-Phelan structure, an idealized foam structure of equal-sized bubbles,[44] was used to mimic the 3-D foam morphology, while the Kelvin structure was adopted to represent the microstructure of PZT (ESI,† Note S1).[45] A representative simulation cell with a characteristic size same as the thickness of the specimens was created by periodically joining the Kelvin cells, as shown in Fig. 2b. Solving the coupled mechanical and electrostatic equilibrium equations with the displacement-controlled boundary conditions yields both the mechanical strain landscape (Fig. 2c) and the electric potential (Fig. 2d) in the composites. The piezoelectric responses (*i.e.*, voltages) were then scaled up from the

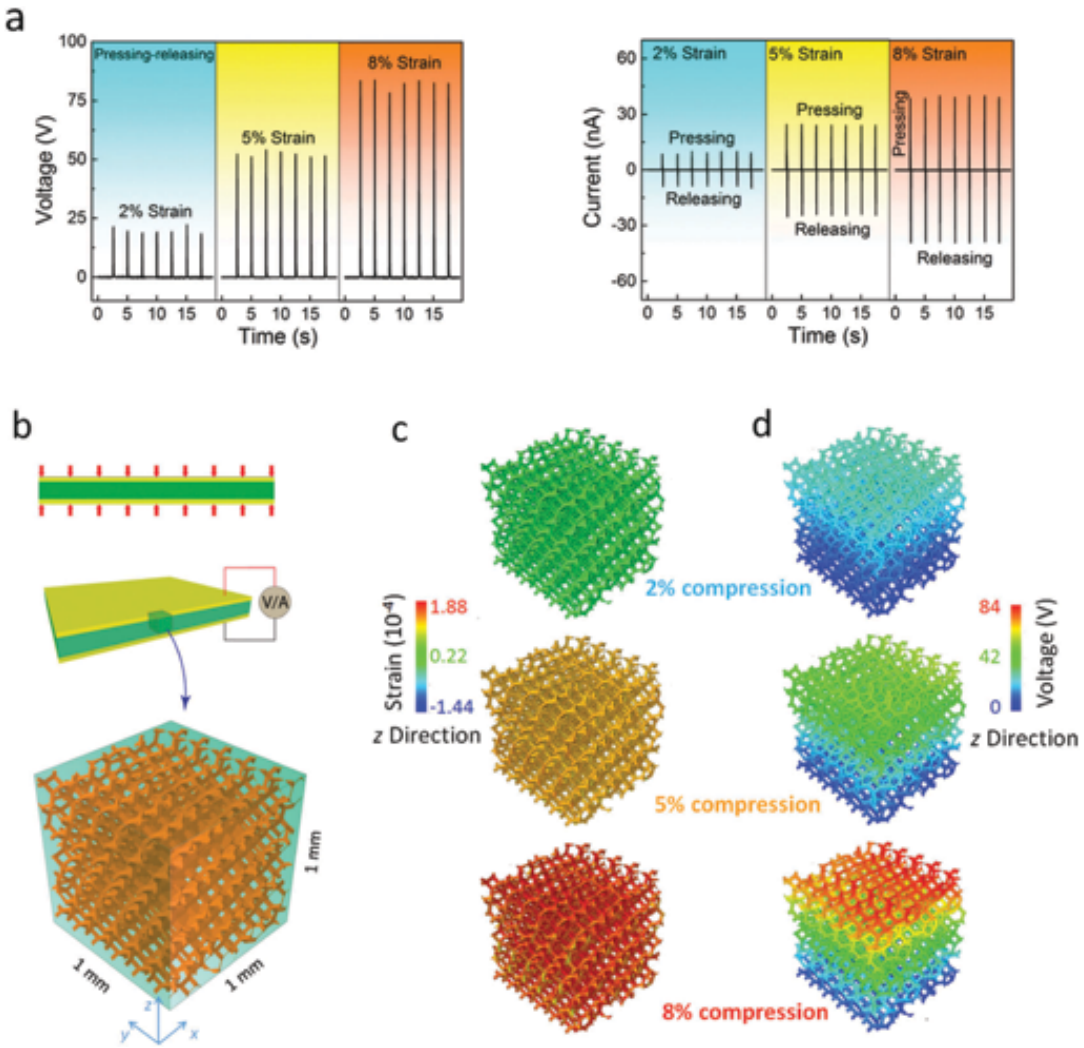

Fig. 2 Experimental and simulated piezoelectric responses of the 3-D composites under compression. (a) The output voltages and currents of the 3-D composites under compression with different compressive strains. (b) Finite element modeling of the representative volume of the composite. (c) The simulated strain field and (d) electric potential on the PZT skeletons when the composites are subjected to 2%, 5% and 8% compressive strains, respectively.

representative cell to the entire composite and compared with the experimental data. The simulated stress/strain field (Fig. 2c) allows us to evaluate the load-transfer efficiency (LTE) from the matrix to the PZT in the composites. On the other hand, the electric field allows us to determine the output voltage (electric potential), given by a line integral $V_E = \int_C \boldsymbol{E} \cdot d\boldsymbol{l}$ across the thickness of the composites along an arbitrary path, where C is an arbitrary path connecting the point with zero potential to the other end. Our finite element simulations show that the calculated output voltages are 21 V, 52 V, and 84 V at 2%, 5%, and 8% applied strains (Fig. 2d and ESI,† Fig. S17, Table S3), respectively, all of which are in good agreement with the experimental data.

In addition to pressing, stretching (Fig. 3a) and bending (Fig. 3c) also generate substantial piezoelectricity in the 3-D composites. For example, a V_{out} ranging from ~22 to ~65 V and an I_{out} between ~25 and ~75 nA are generated when the stretching strain increases from 5% to 15% (Fig. 3a and ESI,† Fig. S18, Table S3). Similar to pressing, we also carried out finite element simulations on the elastic and piezoelectric responses of the composites under stretching (Fig. 3b) and bending (Fig. 3d and ESI,† Fig. S19). For the bending case, the composite resides on an auxiliary substrate to form a film structure. Upon bending, the composite above the neutral axis (the dashed line in Fig. 3d, bottom panel) undergoes tension. Thus piezoelectricity induced by bending (Fig. 3d) is little different from that by stretching (Fig. 3b). Our simulated voltages under stretching and bending agree well with the experimental measurements (ESI,† Fig. S18 and S20). Furthermore, as shown in ESI,† Fig. S21, the 3-D composite produces highly stable V_{out} even after 5000 stretching–releasing cycles of 15% strain, manifesting its high mechanical durability.

2.3 Comparison to the other composites with low-dimensional ceramic fillers

To understand the mechanoelectrical mechanisms underlying the exceptional piezoelectric effect of the 3-D composites, we carried out comparative studies between the 3-D interconnect

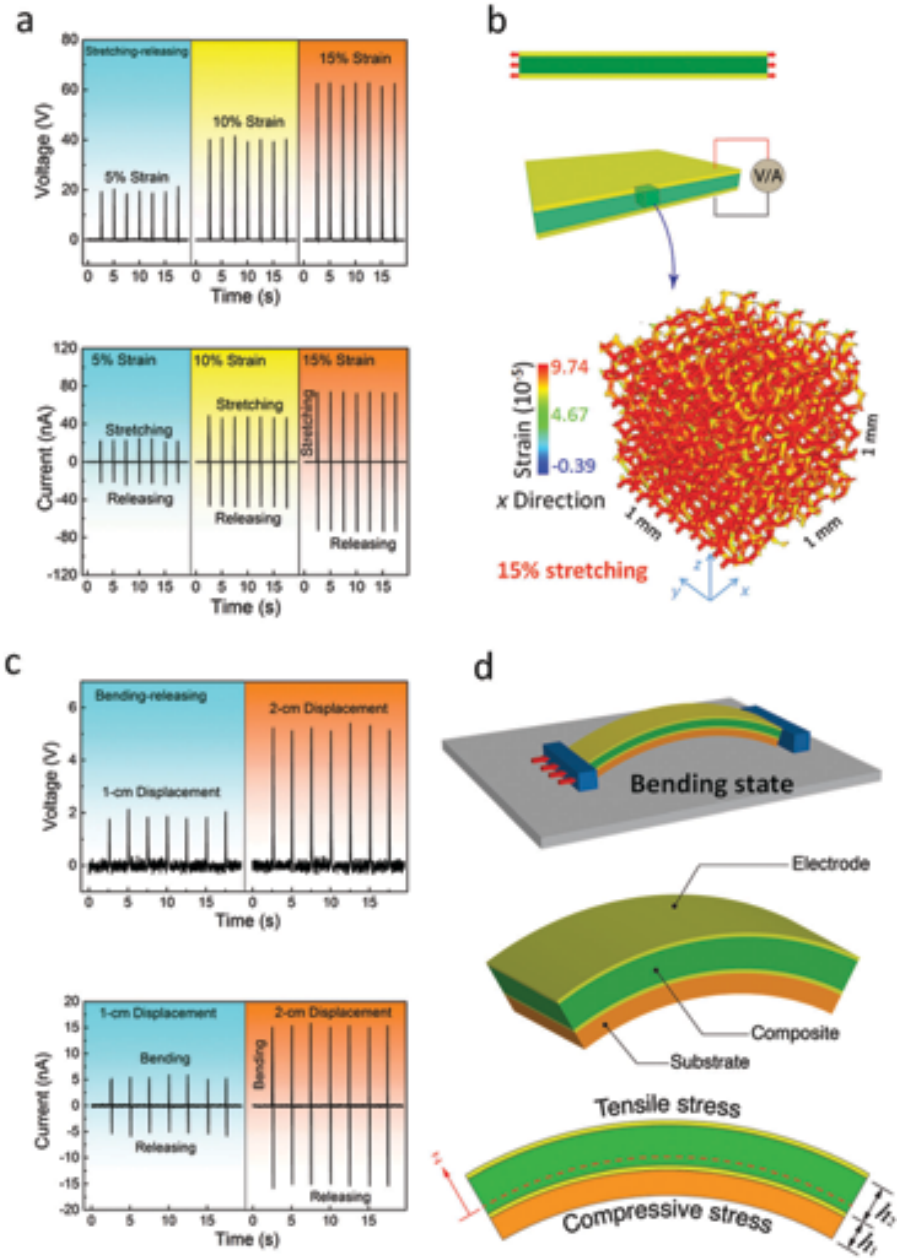

Fig. 3 Experimental and simulated piezoelectric responses of the 3-D composites under stretching and bending. (a) The output voltages and currents of the 3-D composites under different stretching strains. (b) Finite element modeling of the strain distribution on the PZT skeleton when the composite is stretched by 15%. (c) The output voltages and currents of the 3-D composites under bending, realized by in-plane compression of 1 cm and 2 cm from the original length of 5 cm between the two ends. (d) Schematic illustration of the simulation model under bending induced by buckling of the film under compression. The thicknesses of the composite (h_1) and the auxiliary substrate (h_2) are 1 mm and 0.4 mm, respectively. Bending generates tensile stress on the top portion of the film and compressive stress on the bottom, separated by the neutral axis (marked by the red dashed line).

microfoam based composites and other composites with low-dimensional PZT fillers. The reference ceramic-polymer composites are composed of PZT nanoparticles (NPs, 300 nm in diameter) and nanowires (NWs, 100 nm in diameter and 3 μm in length) with the same volume fraction of PZT (*i.e.*, 16 vol%) dispersed in PDMS, as shown in ESI,† Fig. S22. Additionally, the PZT NP composite with 1 wt% multiwall carbon nanotubes (CNTs), labelled as the NP-CNT composite, was also fabricated for comparison. It has been shown that the presence of CNTs can enhance load transfer to the NPs in the polymer composites.[37] The output voltages and currents of the composites were measured when they were subjected to pressing, stretching, and bending. We found that the measured V_{out} and I_{out} from the composites with the low-dimensional PZT fillers are significantly lower than those of the 3-D composites under all the loading cases (pressing, stretching, and bending), as compared in Fig. 4 and ESI,† Table S3. For example, under an 8% compressive strain, V_{out} and I_{out} are 7 V and 0.4 nA, 37 V and 18 nA, and 27 V

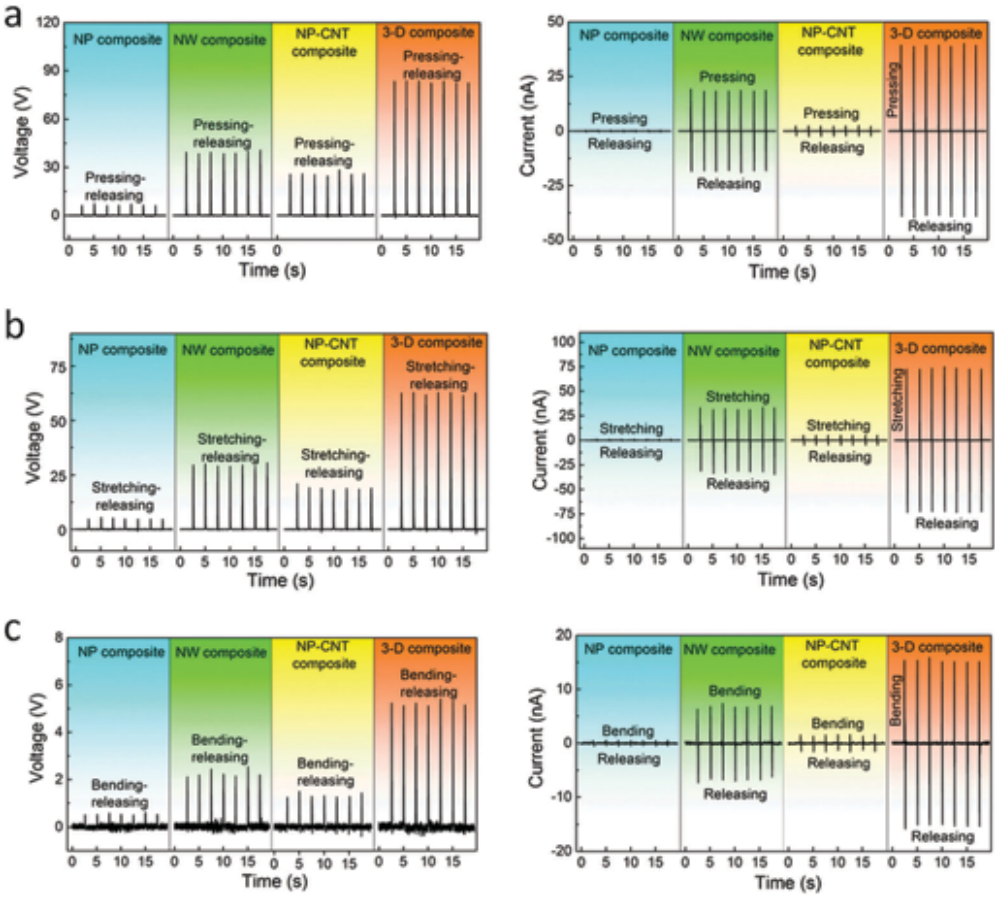

Fig. 4 Piezoelectric responses of the NP, NW, NP-CNT and 3-D composites with multiple deformation modes. (a) The output voltages and currents of different composites under compressing–releasing mode with 8% strain. (b) The output voltages and currents of the composites under stretching–releasing mode with 15% strain. (c) The output voltages and currents of the samples under bending by a displacement of 2 cm from an original length of 5 cm. Overall, the 3-D composites exhibit superior performance compared to the other composites with low-dimensional fillers.

and 2 nA, respectively, for the NP, NW and NP-CNT composites in comparison to 85 V and 40 nA for the 3-D composite (Fig. 4a).

To rationalize the comparatively superior piezoelectric performance of the 3-D composites, we next derive the LTE in these composites from mechanics analysis (see ESI† Note S2). Without loss of generality, we consider the composites undergoing a uniaxial compressive strain ε_{33} in the thickness direction. The LTE is denoted by $\eta \equiv \varepsilon_{33}^{PZT}/\varepsilon_{33}$ $(0 \le \eta \le 1)$, where ε_{33}^{PZT} is the average strain transferred to the PZT fillers. For the NP composites, the LTE is:

$$\eta_{NP} = \frac{\kappa}{1-\phi^{1/3}} \quad (1)$$

where ϕ is the volume fraction of the PZT in the composite, and $\kappa = Y^{PDMS}/Y^{PZT}$ is the ratio of the Young's moduli of the PDMS matrix to the PZT NPs. Note that in eqn (1) $\kappa \ll 1$, η_{NP} is thus limited by the large disparity in the elastic moduli of the PDMS matrix and the PZT NPs. For a typical value κ = 1/60 000 and ϕ = 16%, $\eta_{NP} \simeq 3.6 \times 10^{-5}$ (Table 1). Indeed, our finite element analysis further confirmed that at 8% compressive strain, the calculated strain transferred to the PZT NPs is $\sim 1.4 \times 10^{-6}$–1.3×10^{-5} (ESI,† Fig. S23a), corresponding to a LTE of 1.8×10^{-5}–1.6×10^{-4}, which agrees with the theoretical prediction by eqn (1). In contrast, the strain in the PDMS is calculated to be around 4×10^{-2}, suggesting that most strain is absorbed by the PDMS matrix but cannot be effectively transferred to the PZT fillers. As a result, a very weak piezoelectric voltage of 1.6 mV is generated by each PZT NP (Fig. 4a and ESI,† Fig. S23b). This yields a very low piezoelectric response of 6 V across the entire NP composite (ESI,† Table S3), which also agrees well with the experimental result ($\sim$7 V), as shown in Fig. 4a.

Different from the isotropic NP composites, the LTE of the NW composites is strongly dependent on the loading directions relative to the NW orientation.[46,47] From fundamental mechanics analyses (see ESI† Note S2), the LTEs of the NW composite in the longitudinal ($\eta_{NW,L}$) and transverse ($\eta_{NW,T}$) directions are estimated to be

$$\eta_{NW,L} \simeq \frac{1+2\rho_S}{1-\phi}\kappa; \quad \eta_{NW,T} \simeq \frac{3\kappa}{1-\phi} \quad (2)$$

eqn (2) shows that the LTEs of the NW composites take the similar functional form as that of the NP composites. In addition to the volume fraction ϕ and the stiffness ratio κ,

Table 1 The load-transfer efficiencies of the composites under 8% compressive strain

	NP composite	NW composite (random dispersity)	3-D composite
Load-transfer efficiency	3.6×10^{-5}	4.9×10^{-4}	0.63

the LTE in the longitudinal direction also depends on the slenderness ratio (ρ_S) of the NWs (here $\rho_S = 30$). For randomly oriented NWs, the LTE is taken as the simple rule of mixing: $\eta_{NW} = \frac{3}{8}\eta_{NW,L} + \frac{5}{8}\eta_{NW,T}$.[47] This gives rise to $\eta_{NW} = 4.9 \times 10^{-4}$, which is over one order of magnitude higher than that of the NP composites (Table 1, see ESI† Note S2). Our finite element simulations show that, under a total 8% compression, the PZT NWs experience a compressive strain of $\sim 4 \times 10^{-5}$, indicating a LTE $\sim 5 \times 10^{-4}$, consistent with the theoretical prediction. To further analyze stress and voltage generation in the NW composite, we performed finite element simulations for three typical orientated NWs: 0° (perpendicular to the applied compressive strain), 45° and 90° (parallel to the applied compressive strain). As shown in ESI,† Fig. S23e, the strain on the 45° NWs is larger than that of the 0° NWs but smaller than that of 90° ones. Notably, the strain generated in the 90° NWs is significantly higher than that of the NPs under the same compressive strain, corresponding to a much stronger piezoelectric effect. In contrast, the computed strain in the 0° NWs is comparable to that in NPs, suggesting the same level of piezoelectric effect in the transverse direction of the NW composites as in NP composites. Indeed, as shown in ESI,† Fig. S23i, under the same compressive strain, the aligned NWs experiences a strain as large as 1.0×10^{-4}, generating a stronger piezoelectric signal of 47 V across the composite with the thickness of 1 mm (ESI,† Fig. S23j and Table S3) than that in the composites with randomly oriented NWs.

For the 3-D interconnected composites, the LTE can be obtained from the Banno unit cell model,[48] as:

$$\eta_{3\text{-}D} \simeq \sqrt{\frac{1+\rho_A}{1+3\rho_A}} \quad (3)$$

where ρ_A is the aspect ratio of the microfoam structure, which characterizes the slenderness of the structure. According to the Banno cell structure, the volume fraction is related to aspect ratio of the PZT skeleton $\phi = (1 + 3\rho_A)/(1 + \rho_A)^3$. For $\phi \sim 16\%$ and $\rho_A = 3$, $\eta_{3\text{-}D} \simeq 0.63$, which is several orders of magnitude higher than all the composites with low-dimensional fillers. Interestingly, unlike the NP and NW composites, the LTE for the microfoam-based composites is independent of the stiffness ratio of the constituent materials. This manifests that load transfer to the PZT microfome does not depend on the PDMS matrix since the microfoam itself already forms a 3-D interconnected pathway for efficient load transfer. Our finite element analysis further confirmed that when the specimen (comprised of the 3-D composite sandwiched by buffer layers, see ESI† Note S2) is subjected to 8% compressive strain, a remarkable homogeneous strain of $\sim 1.8 \times 10^{-4}$ is transferred onto the 3-D PZT skeletons (Fig. 2c and ESI,† Fig. S23m). The composite experiences a strain of $\sim 3.2 \times 10^{-4}$, giving rise to an effective LTE of 0.6, consistent with the theoretical prediction. The strain transferred to the PZT microfoam is comparable to that in the longitudinal direction of the NW composites, but over one order of magnitude higher than that of the NPs and the transverse direction of the NW composites (ESI,† Fig. S23a, e and i). The high LTE thus enables the 3-D composites to generate a substantial piezoelectric voltage of 85 V, which is well beyond the capabilities of the currently available composites with NP or NW fillers (Fig. 4a and ESI,† Table S3). It should be noted that even with a load-transfer enhancement CNT network, the piezoelectric response of the NP-CNT composites is still far below that of the 3-D composites (Fig. 4a and ESI,† Table S3).

We subsequently simulated the strain distribution in the 3-D composites when subjected to 15% stretching strain along the x direction (the direction parallel to the stretching force), and analyzed their piezoelectric responses (ESI,† Fig. S23c, g, k and o). Due to the isotropic PZT skeletons and their composites, the applied stretching strain on the 3-D composites is effectively transferred to the active PZT foams, showing the similar strain-transfer capability in the compressing mode. As manifested in Fig. 3b and ESI,† Fig. S23o, a high stretching strain around 1.0×10^{-4} is able to be directly transferred to the 3-D skeleton (Fig. 3b and ESI,† Fig. S23o), which is 5 times greater than the strain applied on the NPs (ESI,† Fig. S23c), creating a high piezoelectric voltage of ~ 65 V similar to the compressing mode in the 3-D composite (Fig. 4b and ESI,† Table S3). In comparison, the local strain of the NWs relies strongly on their orientations. Under the stretching mode, the NWs lying along the x-axis is significantly higher than those orientated along other directions (ESI,† Fig. S23g). The stimulated piezoelectric voltage of the NW composites with randomly dispersed NWs is ~ 5 times higher than that of the NP composites, but significantly lower than that of the 3-D composites (ESI† Table S3). It is worth pointing out that while the vertically aligned NW composites have a relatively strong piezoelectric response than the composites with randomly dispersed NWs under compressive mode, the anisotropic geometry is unfavorable for the stretching mode (ESI,† Fig. S23k). Indeed, under stretching the piezoelectric response of the vertically aligned NW composites is only half of that of the randomly dispersed NW composites under the same applied stretching strain (ESI,† Fig. S23l and Table S3).

2.4 Pyroelectric energy harvesting

The 3-D composites were also found to exhibit superior pyroelectricity, *i.e.*, the generation of electric signals in response to temperature fluctuation. Upon a temperature rise from 25 °C to 35 °C ($\Delta T = 10$ °C), the pyroelectric V_{out} and I_{out} of 1.6 V and 100 pA, respectively, were generated from the 3-D composites, as shown in Fig. 5a, b and ESI,† Fig. S24. After reversely connecting the composites to the measurement system, the obtained signals switched the sign, confirming the pyroelectric nature of the measured signals (ESI,† Fig. S25). The pyroelectric effect generated by the 3-D composites is several-fold higher

than the composites with low-dimensional PZT fillers under the same range of temperature variations, as shown in ESI,† Fig. S26.

Similar to the highly efficient mechanical load transfer, the 3-D interconnected PZT skeleton forms continuous conductive pathways (the heat conductivity of PZT ceramic is $\sim$1.2 W m^{-1} K^{-1}, 8 times that of the PDMS matrix),[49] giving rise to the improved heat transfer and thus enhanced pyroelectric performance. Fig. 5c shows our finite element results on the temperature distribution of the composites with different ceramic fillers (see ESI† Notes S3). Our simulation results reveal that once the heat penetrates the outermost layers of the PDMS matrix and enters the PZT skeletons, the heat can unimpededly flux through the interconnected 3-D ceramic networks, leading to a fast and homogeneous temperature change of the composites within a short time interval of 1 s. As a result, a sizable pyroelectric voltage of 1.6 V is attained in the 3-D composites (Fig. 5). In contrast, within the same time period, only a thin bottom layer of the NP composites close to the heat source is heated up. Similar to the strain-transfer process, the discrete NPs can only absorb the heat from the surrounding PDMS matrix, which serves as a thermal-insulation medium rather a thermal conduction channel in heat transfer (Fig. 5c). Therefore, only very few PZT NPs located at the bottom of the composites can be heated up to generate pyroelectric signals within the same time period. As validated by the experimental results, the pyroelectric voltages in the NP and NP-CNT composites are only a small fraction of that in the 3-D composites under the same temperature fluctuation (ESI,† Fig. S26). The NW composites exhibit better heat transfer efficiency than the NP composites, especially in the longitudinal direction of the NWs. However, the discontinuity of the ceramic phase also renders a lower pyroelectric response (V_{out} = 0.8 V) than the 3-D composites.

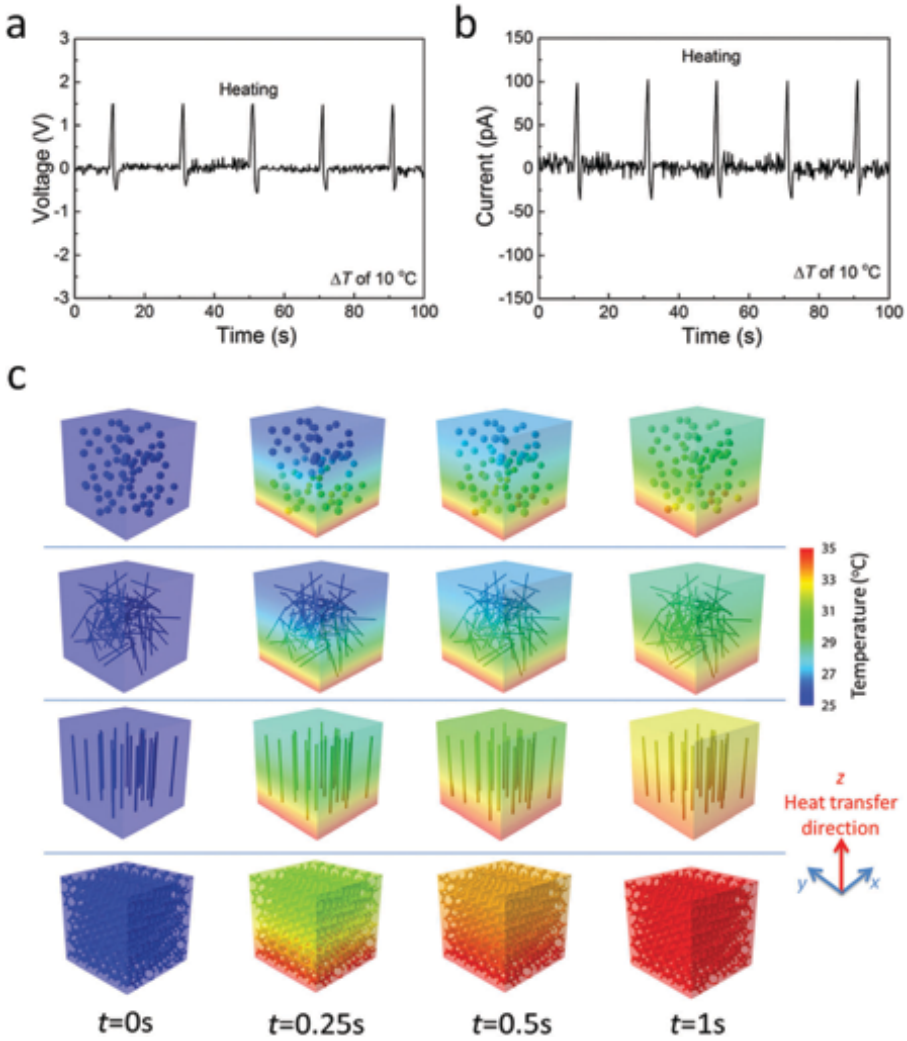

Fig. 5 Pyroelectric responses of the composites. (a and b) The pyroelectric output voltage and current of the 3-D composites under a temperature fluctuation of 10 °C. (c) Finite element modeling of the heat transfer in the composites with different ceramic fillers. A hot plate as a heat source of a temperature 35 °C, 10 °C higher than the ambient temperature, is placed at the bottom of the composites. Heat transfers along the *z* direction from the bottom to the top of the samples. For each type of ceramic fillers, four different snapshots in the heat transfer process are displayed. The 3-D interconnected PZT ceramic-based composite exhibits significantly faster heat transfer than other composites.

2.5 Concurrent piezo-/pyro-electric energy harvesting

To examine the performance of the 3-D composites under complex thermomechanical loading conditions, the piezoelectric V_{out} was measured under 8% compressive strain after the composite was subjected to 2000 heating–cooling (25 °C–35 °C) cycles (Fig. 6a). No noticeable decay in V_{out} was observed due to the cycling. Similarly, the pyroelectric V_{out} remained unchanged under thermal heating after 2000 pressing–releasing cycles (8% compressive strain), as shown in Fig. 6b. These experiments demonstrate that thermal and mechanical cycling does not interfere the subsequent piezo and pyroelectric responses of the 3-D composites.

We then explored the coupled piezoelectric and pyroelectric effects by applying mechanical and thermal stimuli synchronously. As shown in Fig. 6c, pyroelectric V_{out} of ~1.6 V was obtained under the heating–cooling cycles with a ΔT of 10 °C, while piezoelectric V_{out} of ~5 V was attained under the pressing–releasing cycles (0.5% compressive strain). Subsequently, simultaneous application of strain and thermal gradients generated a superimposed output V_{out} of ~6.5 V from a single 3-D composite. This superimposable piezo/pyroelectric effect enables concurrent thermal and mechanical energy harvesting.

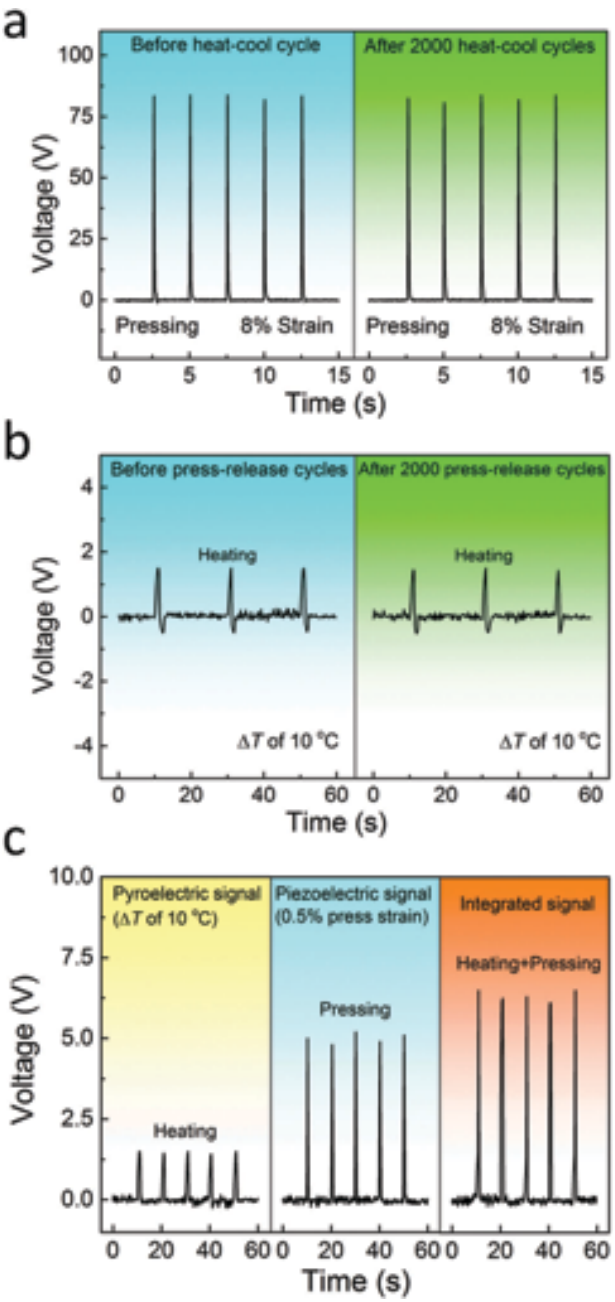

Fig. 6 Pyroelectric, pyroelectric and concurrent piezo-/pyro-electric responses of the 3-D composites. (a and b) The piezoelectric and pyroelectric voltages of the 3-D composites before and after 2000 heating–cooling cycles (ΔT of 10 °C) and 2000 pressing–releasing cycles (8% strain), respectively. (c) The individual and integrated piezoelectric–pyroelectric output voltages of the 3-D composites, showing the superimposable piezo/pyroelectric effect.

3. Conclusions

We have developed a new class of flexible and durable ceramic-polymer composites, which feature 3-D cellular-structured foams as the piezoceramic fillers. Our experimental characterizations suggest that the 3-D PZT foam composites exhibit significantly improved piezoelectric and pyroelectric effects as compared to the traditional piezoelectric polymer composites with low-dimensional ceramic fillers. The 3-D composite is able to generate stable output voltages over thousands of mechanical and thermal cycles, demonstrating its great compliance, stability, and durability. Comprehensive theoretical and numerical studies reveal that the 3-D PZT skeleton constitutes a continuous pathway for load and heat transfer, which explains the exceptional piezo/pyroelectricity of the composite. In contrast, the large stiffness disparity of the ceramic fillers and the polymer matrix and discontinuity of the ceramic phase of the composites with low-dimensional ceramic fillers are the critical factors limiting their load- and heat-transfer efficiency, and subsequently piezoelectric and pyroelectric effects. We further demonstrated that the piezoelectric and the pyroelectric responses are superimposable in the 3-D composites, thereby enabling highly efficient concurrent thermal and mechanical energy harvesting. Our collective results suggest widespread applications of the 3-D interconnected microfoam based composites as sensory and power-generation components in human motion monitoring devices, robotics, and artificial muscles and skins.

4. Experimental section

Preparation of the PZT microfoams and its 3-D composites

The PZT [$Pb(Zr_{0.52}Ti_{0.48})O_3$] microfoams were fabricated by a sol–gel method with PU foam templates (commercially available cleanroom wiper, TX704, ITW Texwipe, ESI,† Fig. S5). For the PZT sol solution (0.1 M), the lead(II) acetate trihydrate (Sigma-Aldrich, 99.5%) was dissolved in acetic acid (Sigma-Aldrich, 99%) under vigorous stirring at 80 °C until the mixture became transparent. After cooling down, the zirconium(IV) propoxide (Aldrich, 70 wt% in 1-propanol) and titanium(IV) butoxide (Alfa, 99%) were added into the transparent solution under constant stirring. 20 mol% excess Pb was introduced to compensate the

lead volatilized during the high-temperature sintering process (ESI,† Fig. S8–S10 and Table S2). Ethylene glycol (Sigma, 99.5%) was then added to the solution to stabilize the PZT sol. After stirring at room temperature for 1 hour, PU foams were immersed in the sol for several minutes. When the polyurethane (PU) foam template was immersed into the PZT sol, the sol was absorbed by the PU template *via* the capillary effect.[50,51] Subsequently, the saturated PU foams were squeezed and dried at 60 °C for 1 hour (ESI,† Fig. S6). During the squeezing step, the excessive sol was extruded from the PU foam with the remaining sol wrapped over the PU form skeletons. The sol wrapped on the PU foam skeletons was converted into gel after drying. Compared to the pristine PU foam, the weight of the template with the converted PZT gel is increased 35%. Note that without squeezing, the excessive PZT sol blocks the pores of the PU template, yielding undesirable microstructures of the PZT ceramic network with closed pores after sintering (ESI,† Fig. S7). The samples were then sintered at around 1000 °C for 2 hours, to yield the PZT 3-D ceramic microfoams. The volume ratio (r_{foam}) of the prepared PZT ceramic foam was calculated according to the equation: $r_{foam} = m_{foam}/(D_T \times V_{foam})$, where m_{foam} and V_{foam} are the mass and volume of the samples, respectively, and D_T is the theoretical density of the $Pb(Zr_{0.52}Ti_{0.48})O_3$ ceramic (*i.e.* 8.05 g cm^{-3}).[52] The PZT ratio of the prepared 3-D ceramic foam is thus estimated to be ~16 vol%. The 3-D PZT/PDMS composites were fabricated by filling PDMS (Sylgard, 184 silicone elastomer kit) into the 3-D PZT ceramic microfoams. The PDMS monomer with 10 wt% curing agent was homogeneously mixed and dropped slowly on the top of the PZT until the PDMS fully penetrated in and covered the ceramic foams. The 3-D composites were obtained after the solidification of the PDMS matrix (annealing in air at 60 °C for 12 hours).

Preparation of the low-dimensional PZT composites

For the comparison purpose, NP, NW and NP-CNT composites with 16 vol% PZT as references have been prepared. The PZT NPs were synthesized *via* a typical sol–gel process. Lead(II) acetate trihydrate (Sigma-Aldrich, 99.5%) and titanium(IV) isopropoxide (Sigma-Aldrich, 99.5%) were dissolved in deionized water and ethanol, respectively. The two solutions were mixed after stirring for 20 minutes. Thereafter, citric acid aqueous solution (1.5 times in mole ratio to the total metal cation content) was added to the mixed Pb and Ti solution. Ammonia solution (Sigma-Aldrich, 0.5 M) was introduced into the mixture to tune the pH value to ~5. Subsequently, the zirconium(IV) oxide (Aldrich) was added to the sol. After a 30 minutes stirring and 2 hours ball milling, the slurry was sonicated (tip-type sonication) and dried at 120 °C overnight. The obtained gel was then calcined at 800 °C for 2 hours, yielding the PZT NPs.

The PZT NWs were fabricated through a hydrothermal method. Firstly, titanium(IV) butoxide (Alfa, 99%) was added into ethanol (0.08 M), and zirconyl chloride octahydrate (Sigma-Aldrich, 98%) was added into deionized water (0.1 M), respectively. The two solutions were mixed and co-precipitated with a 0.15 M ammonia solution (Sigma-Aldrich, 0.5 M). The obtained $Zr_xTi_{1-x}O_2{\cdot}nH_2O$ gel was washed and dispersed in deionized water. Subsequently, a lead(II) nitrate (Sigma-Aldrich, 99%) solution (0.11 M) with 0.5 M potassium hydroxide (Sigma-Aldrich, 90%) and 0.4 g L^{-1} of poly(vinyl alcohol) (PVA, Aldrich, 99%) was dissolved in the $Zr_xTi_{1-x}O_2{\cdot}nH_2O$ solution. The mixture was filled in an autoclave (PARR 4748A, 200 mL) with a Teflon liner. For the hydrothermal reaction, the solution in the vessel was kept at ~200 °C for about 4 hours with stirring. Then, precipitated PZT NWs were washed with deionized water for several times and dried at 60 °C. The resulting NWs were finally heated at 650 °C for 2 h.

The NP, NW and NP-CNT composites were made by mixing the PZT NPs (16 vol%), NWs (16 vol%) and PZT NPs (16 vol%) + multiwall CNT (1 wt%, Aldrich, 98%) with PDMS, respectively. With 10 wt% curing agent, the PDMS-PZT mixtures were sonicated (tip-type sonication) for 10–30 minutes for homogeneous dispersion of the fillers. The mixtures were then cast in molds and held at 60 °C for 12 hours.

Characterization

XRD diffraction patterns were acquired by using a PANalytical Xpert pro MPD. The microstructures of the samples were observed with a Hitachi S-4800 FE-SEM. The element composition of the PZT ceramic microfoams was studied with the energy dispersive X-ray spectroscopy (EDS, GENESIS), electron probe microanalysis (EPMA 8050G, SHIMADZU) and X-ray photoelectron spectroscopy (XPS, Thermo Fisher Scientific ESCALAB 250Xi). The polarization–electric field (*P–E*) loops were measured by the Sawyer-Tower circuit. For piezoelectric and pyroelectric characterizations, the samples were poled at 120 °C with an electric field of 150 kV cm^{-1} (along the out-of-plane direction) for 15 hours.

Conflicts of interest

There are no conflicts to declare.

Acknowledgements

G. Z. gratefully acknowledges the support from the National Science Foundation of China (51772108, U1532146 and 61675076) and the National Key Research and Development Program of China (2016YFB0402705). S. L. Z. acknowledges the support by the National Science Foundation through the projects CMMI-0900692, DMR-1610430, and ECCS-1610331. G. Z. would also like to acknowledge the support from the Analytical and Testing Center, Huazhong University of Science and Technology.

Notes and references

1 F. R. Fan, W. Tang and Z. L. Wang, *Adv. Mater.*, 2016, **28**, 4283.
2 S. Park, H. Kim, M. Vosgueritchian, S. Cheon, H. Kim, J. H. Koo, T. R. Kim, S. Lee, G. Schwartz, H. Chang and Z. Bao, *Adv. Mater.*, 2014, **26**, 7324.
3 H. Wu, Y. A. Huang, F. Xu, Y. Q. Duan and Z. P. Yin, *Adv. Mater.*, 2016, **28**, 9881.

4 A. Erturk and D. J. Inman,*Piezoelectric energy harvesting*, John Wiley and Sons, Ltd., 2011.
5 C. R. Bowen, H. A. Kim, P. M. Weaver and S. Dunn, *Energy Environ. Sci.*, 2014, **7**, 25.
6 J. Briscoe and S. Dunn, *Nano Energy*, 2015, **14**, 15.
7 C. Dagdeviren, Z. Li and Z. L. Wang, *Annu. Rev. Biomed. Eng.*, 2017, **19**, 85.
8 Y. Qi and M. C. Mcalpine, *Energy Environ. Sci.*, 2010, **3**, 1275.
9 T. Q. Trung and N. E. Lee, *Adv. Mater.*, 2016, **28**, 4338.
10 L. Persano, C. Dagdeviren, Y. Su, Y. Zhang, S. Girardo, D. Pisignano, Y. Huang and J. A. Rogers, *Nat. Commun.*, 2013, **4**, 1633.
11 J.-H. Lee, K. Y. Lee, M. K. Gupta, T. Y. Kim, D.-Y. Lee, J. Oh, C. Ryu, W. J. Yoo, C.-Y. Kang, S.-J. Yoon, J.-B. Yoo and S.-W. Kim, *Adv. Mater.*, 2014, **26**, 765.
12 C. L. Sun, J. Shi, D. J. Bayerl and X. D. Wang, *Energy Environ. Sci.*, 2011, **4**, 4508.
13 Z. Zhang, C. Yao, Y. Yu, Z. Hong, M. Zhi and X. Wang, *Adv. Funct. Mater.*, 2016, **26**, 6760.
14 D. Zabek, J. Taylor, E. L. Boulbar and C. R. Bowen, *Adv. Energy Mater.*, 2015, **5**, 1401891.
15 S. Horiuchi and Y. Tokura, *Nat. Mater.*, 2008, **7**, 357.
16 D. Damjanovic, *J. Am. Ceram. Soc.*, 2005, **88**, 2663.
17 A. Koka, Z. Zhou and H. A. Sodano, *Energy Environ. Sci.*, 2014, **7**, 288.
18 S. Xu, B. J. Hansen and Z. L. Wang, *Nat. Commun.*, 2010, **1**, 93.
19 A. Koka and H. A. Sodano, *Nat. Commun.*, 2013, **4**, 2682.
20 G. Zhang, X. Zhang, H. Huang, J. Wang, Q. Li, L.-Q. Chen and Q. Wang, *Adv. Mater.*, 2016, **28**, 4811.
21 C. Dagdeviren, B. D. Yang, Y. Su, P. L. Tran, P. Joe, E. Anderson, J. Xia, V. Doraiswamy, B. Dehdashti, X. Feng, B. Lu, R. Poston, Z. Khalpey, R. Ghaffari, Y. Huang, M. J. Slepian and J. A. Rogers, *Proc. Natl. Acad. Sci. U. S. A.*, 2014, **111**, 1927.
22 G.-T. Hwang, H. Park, J.-H. Lee, S. Oh, K.-I. Park, M. Byun, H. Park, G. Ahn, C. K. Jeong, K. No, H. Kwon, S.-G. Lee, B. Joung and K. Jae, *Adv. Mater.*, 2014, **26**, 4880.
23 Y. Qi, J. Kim, T. D. Nguyen, B. Lisko, P. K. Purohit and M. C. McAlpine, *Nano Lett.*, 2011, **11**, 1331.
24 M.-H. Seo, J.-Y. Yoo, S.-Y. Choi, J.-S. Lee, K.-W. Choi, C. K. Jeong, K. J. Lee and J.-B. Yoon, *ACS Nano*, 2017, **11**, 1520.
25 G.-T. Hwang, V. Annapureddy, J. H. Han, D. J. Joe, C. Baek, D. Y. Park, D. H. Kim, J. H. Park, C. K. Jeong, K.-I. Park, J.-J. Choi, D. K. Kim, J. Ryu and K. J. Lee, *Adv. Energy Mater.*, 2016, **6**, 1600237.
26 C. K. Jeong, S. B. Cho, J. H. Han, D. Y. Park, S. Yang, K.-I. Park, J. Ryu, H. Sohn, Y.-C. Chung and K. J. Lee, *Nano Res.*, 2017, **10**, 437.
27 Y. Y. Yang, H. Zhang, G. Zhu, S. Lee, Z. H. Lin and Z. L. Wang, *ACS Nano*, 2013, **7**, 785.
28 S. H. Bhang, W. S. Jang, J. Han, J. K. Yoon, W.-G. La, E. Lee, Y. S. Kim, J.-Y. Shin, T.-J. Lee, H. K. Baik and B.-S. Kim, *Adv. Funct. Mater.*, 2017, **27**, 1603497.
29 M. Ha, S. Lim, J. Park, D. S. Um, Y. Lee and H. Ko, *Adv. Funct. Mater.*, 2015, **25**, 2841.
30 T. Furukawa, K. Ishida and E. Fukada, *J. Appl. Phys.*, 1980, **51**, 4561.
31 T. Furukawa, K. Fujino and E. Fukada, *Jpn. J. Appl. Phys.*, 1976, **15**, 2119.
32 C. K. Jeong, J. Lee, S. Han, J. Ryu, G. T. Hwang, D. Y. Park, J. H. Park, S. S. Lee, M. Byun, S. H. Ko and K. J. Le, *Adv. Mater.*, 2015, **27**, 2866.
33 Y. Yang, J. H. Jung, B. K. Yun, F. Zhang, K. C. Pradel, W. Guo and Z. L. Wang, *Adv. Mater.*, 2012, **24**, 5357.
34 X. Chen, S. Y. Xu, N. Yao and Y. Shi, *Nano Lett.*, 2010, **10**, 2133.
35 J. J. H. Jung, M. Lee, J. I. Hong, Y. Ding, C. Y. Chen, L. J. Chou and Z. L. Wang, *ACS Nano*, 2011, **5**, 10041.
36 B. Ploss, B. Ploss, F. G. Shin, H. L. W. Chan and C. L. Choy, *Appl. Phys. Lett.*, 2000, **76**, 2776.
37 K. Park, M. Lee, Y. Liu, S. Moon, G. T. Hwang, G. Zhu, J. E. Kim, S. O. Kim, D. K. Kim, Z. L. Wang and K. J. Lee, *Adv. Mater.*, 2012, **24**, 2999.
38 Z. Zhou, H. Tang and H. A. Sodano, *Adv. Mater.*, 2014, **26**, 7547.
39 A. K. Naskar, J. K. Keum and R. G. Boeman, *Nat. Nanotechnol.*, 2016, **11**, 1026.
40 K. Kim, W. Zhu, X. Qu, C. Aaronson, W. R. McCall, S. Chen and D. J. Sirbuly, *ACS Nano*, 2014, **8**, 9799.
41 L. R. Meza, S. Das and J. R. Greer, *Science*, 2014, **345**, 1322.
42 S. H. Shin, Y. H. Kim, M. H. Lee, J. Y. Jung and J. Nah, *ACS Nano*, 2014, **8**, 2766.
43 S. Xu, Y. Yeh, G. Poirier, M. C. McAlpine, R. A. Register and N. Yao, *Nano Lett.*, 2013, **13**, 2393.
44 D. Weaire and R. A. Phelan, *Philos. Mag. Lett.*, 1994, **96**, 107.
45 D. Weaire, *J. Phys.: Conf. Ser.*, 2009, **158**, 012005.
46 Y. B. Lee, J. K. Han, S. Noothongkaew, S. K. Kim, W. Song, S. Myung, S. S. Lee, J. Lim, S. D. Bu and K.-S. An, *Adv. Mater.*, 2017, **29**, 1604500.
47 J. C. H. Affdl and J. L. Kardos, *Polym. Eng. Sci.*, 1976, **16**, 344.
48 C. R. Bowen, A. Perry, H. Kara and S. W. Mahon, *J. Eur. Ceram. Soc.*, 2001, **21**, 1463.
49 B. M. Foley, *J. Appl. Phys.*, 2017, **121**, 205104.
50 S. Kobayashi and B. Zeegers, *J. Cell. Plast.*, 1988, **24**, 80.
51 J. Ha, J. Kim, Y. Jung, G. Yun, D.-N. Kim and H.-Y. Kim, *Sci. Adv.*, 2018, **4**, eaao7051.
52 C. L. Huang, B. H. Cheng and L. Wu, *Mater. Res. Bull.*, 2004, **39**, 523.